Corrosion Science 157 (2019) 31–40

Contents lists available at ScienceDirect

Corrosion Science

journal homepage: www.elsevier.com/locate/corsci

Investigation of iron passivity in highly alkaline media using reactive-force field molecular dynamics

Hossein DorMohammadi[a], Qin Pang[b], Pratik Murkute[c], Líney Árnadóttir[b], O. Burkan Isgor[a,*]

[a] Oregon State University, School of Civil and Construction Engineering, Corvallis, Oregon, USA
[b] Oregon State University, School of Chemical, Biological and Environmental Engineering, Corvallis, Oregon, USA
[c] Oregon State University, Materials Science Program, Mechanical, Industrial and Manufacturing Engineering, Corvallis, Oregon, USA

ARTICLE INFO

Keywords:
Iron passivity
Alkaline electrolyte
Molecular dynamics (MD)
Reactive Force Field (ReaxFF)
X-ray photoelectron spectroscopy (XPS)

ABSTRACT

The passivity of Fe(110) in a 0.316 M NaOH solution (pH = 13.5) was investigated using Reactive Force Field Molecular Dynamics. The initial stages of passivation involved the formation of $Fe(OH)_2$ species on the metal surface, which created conditions for oxygen diffusion into the metal without iron dissolution into the electrolyte. The passive film had multiple oxide structures: Fe_2O_3 in outer layers, Fe_3O_4 in the middle layers, and FeO in the innermost layers. A parallel XPS investigation showed that the Fe^{III}/Fe^{II} ratio decreased with increasing film depth and confirmed the findings of the ReaxFF-MD simulations.

1. Introduction

In highly alkaline electrolytes (pH > ~12), iron is covered with a passive film that protects the metal from active corrosion [1,2]. This thermodynamic property of iron enables the use of carbon steel (which typically has 0.2–0.4% of carbon by mass) in concrete as reinforcement [3–6]. However, the passive film can break down in the presence of chlorides-containing salts or pH-reducing processes. The breakdown of passivity (depassivation) may lead to higher rates of metal loss (active corrosion) and, in the case of carbon steel reinforced concrete, is a great concern for the structural integrity of structures [3–6].

The passivity and chloride-induced depassivation of carbon steels and iron in high pH environments have been extensively studied using electrochemical methods. These techniques provided valuable information about the average electrochemical behavior in different environments ranging from simulated concrete pore solutions to more realistic conditions [7–17]. Previous microscopic studies have also shown that the passive films that form on carbon steel and iron in alkaline environments are typically 3-15-nm thick [18–20]. Several researchers used nanoscale surface characterization techniques to develop a fundamental understanding of the mechanisms of the passivity of iron and steel in alkaline environments. For example, Sanchez et al. [21,22] proposed a model that was based on a two-layered film: The inner layer was composed of mixed iron oxides with a stoichiometry similar to that of magnetite (i.e., Fe_3O_4 or FeO + Fe_2O_3), where oxidation and reduction processes take place between the iron substrate and the Fe^{II} oxides. It was hypothesized that passivity was mainly related to the formation of the Fe^{II} oxide layer and the outer layer was mainly composed of Fe^{III} oxides. This two-layer model is in agreement with theoretical passivity models that are based on an inner barrier layer formed directly on the metal substrate, and an outer layer that precipitates through hydrolysis of cations ejected from the inner layer [23,24].

A number of other studies provided evidence for this two-layer passivity model. Joiret et al. [25] made similar observations to those of Sanchez et al. [21,22] using in-situ Raman spectroscopy on the passive film structure of carbon steel exposed to NaOH solutions. Additionally, Ghods et al. [18–20,26] investigated the nano-scale properties of passive films that form on carbon steel in simulated concrete pore solutions using multiple techniques including transmission electron microscopy (TEM) [18], X-ray photoelectron spectroscopy (XPS) [19,20], and electron energy-loss spectroscopy (EELS) [26]. These studies showed that oxide films that form on carbon steel in simulated concrete pore solutions were composed of multiple oxide/hydroxide layers with a total thickness of 3–15 nm. XPS studies [19,20] showed that the inner film was mainly composed of Fe^{II} oxides while the outer region consisted mostly of Fe^{III} oxides. EELS study [26] provided additional evidence that the films formed on carbon steel in simulated concrete pore solutions contained indistinctly layered regions. Regardless of the simulated pore solution used for passivation, the inner regions were mainly composed of FeO, which is protective in alkaline media [27]. Above this layer, some traces of Fe_3O_4 were found in the intermediate

---

[*] Corresponding author.
E-mail address: burkan.isgor@oregonstate.edu (O. Burkan Isgor).

https://doi.org/10.1016/j.corsci.2019.05.016
Received 2 November 2018; Received in revised form 16 April 2019; Accepted 15 May 2019

region, while FeO was less evident. The outer regions of the oxide film contained Fe_3O_4, and α-Fe_2O_3, but the composition of this layer was affected by the composition of the simulated pore solution used in the experiments.

Even though these nano-scale surface characterizations studies provide valuable information about the structure of the passive films that form on carbon steel (and iron) in alkaline electrolytes, they cannot adequately explain the dynamic processes that lead to their formation, but that understanding is critical in explaining their resistance to depassivating processes. Unfortunately, most current experimental techniques that can give in-situ and real-time detailed dynamic information about these electrochemical processes provide limited information on the nanometer scale. Atomistic modeling techniques, such as Reactive Force Field Molecular Dynamics (ReaxFF-MD) [28–37] and Density Functional Theory (DFT) [38–43], have shown great potential to develop such fundamental understanding. In particular, ReaxFF-MD has emerged as a simulation framework to investigate reactive processes in relatively large scales that can be correlated to physical systems.

For example, Assowe et al. [34] investigated the interaction of a nickel substrate with water molecules using ReaxFF-MD. Their results supported the expected thermodynamic behavior of nickel in pure water. Different steps of nickel oxidation including adsorption, dissociation of water, deprotonation, dissolution, and growth of hydroxide/oxide were simulated successfully. Similarly, Russo et al. [31] used ReaxFF-MD to examine the reaction dynamics associated with the dissociation of water on aluminum, and Jeon et al. [32] followed a similar approach to study the interaction of copper substrates and chlorine under aqueous conditions. Despite its growing utilization to investigate the oxidation processes of non-ferrous metals [31–35], ReaxFF-MD has seen only limited use to study electrochemical processes that take place on iron [44–46]. Pan and van Duin [44] and Pan [45] demonstrated the feasibility of using ReaxFF-MD in simulating iron oxidation at the iron-water ($pH = 7$) interface. These simulations identified different stages of iron oxidation based on the generated chemical species. In a recent study, DorMohammadi et al. [46] simulated the initial stages of iron corrosion in a neutral electrolyte ($pH = 7$). This study showed that the oxide film formed was not protective and contained a mixture of oxides, which are in agreement with experimental data [2]. In a recent review paper, Belonis et al. showed the feasibility of studying iron passivation in high pH electrolytes using ReaxFF-MD [47].

The main objective of this research is to simulate the passivation process of pure iron in a highly alkaline environment (0.316 M NaOH solution; $pH = 13.5$) using ReaxFF-MD and provide detailed compositional information of the oxide films formed during the passivation process. Parallel XPS and electrochemical investigations were performed on 99.95% pure iron specimens to support the simulations. Although the electrolyte was chosen to match the pH of typical concrete pore solutions, we acknowledge that real concrete pore solutions are complex and contain several other ions such as Ca^{+2}, K^{+}, $(SO_4)^{-2}$ [20]. These ions are known to affect the passivation process and the properties of the passive film, as also shown in an earlier work of one of the co-authors [7]; however, here we study a simplified electrolyte to gain fundamental understanding into the dynamic processes that lead to passivation in simple high pH electrolytes. Similar concerns were behind the reason for choosing pure iron, rather than carbon steel, as the subject of investigation. Although carbon steel passivates slower than iron [48], and the critical chloride threshold of carbon steel is typically smaller than that of iron [11,49], the passivation and depassivation mechanisms of both are considered to be driven by iron interactions with the electrolyte. This assumption is justified by several electrochemical and thermodynamic studies that indicate that passivation and chloride-induced depassivation of carbon steel is mainly driven by the interaction of iron with the electrolyte [1,2].

2. Materials and methods

2.1. ReaxFF-MD simulations

The simulated system involved a Fe(110) structure (24.61 Å x 20.40 Å x 22.87 Å) containing 1080 Fe atoms, which was exposed to a pH 13.5 NaOH solution. The electrolyte was simulated using 21 Na and OH ions distributed evenly in equally spaced seven layers of 348 water molecules. Previous studies have shown that different surface orientations have little effect on the oxidation behavior of iron [46,50–55]; therefore, the Fe(110) was used here to represent a closely packed iron surface. Periodic boundary conditions were applied along x and y directions, while fixed boundary condition was imposed along the z direction. A reflecting wall was applied at the end of the solution domain in order to confine the electrolyte and to avoid the interactions of the solution with the bottom of the periodic surface slab.

Simulations were performed using the Large-scale Atomistic/Molecular Massively Parallel Simulator (LAMMPS) framework [56] and the Extreme Science and Engineering Discovery Environment (XSEDE) [57]. The ReaxFF framework was based on the interatomic potential theory developed by van Duin et al. [58]. The detailed explanation of the framework is not provided here for brevity but can be found in other references [31,59–67]. The specific ReaxFF parameters for iron and other interacting species (e.g., Na, O, H) (i.e., parameters required for determining bond order, bond energy, valence angle energy, torsional angle energy, and van der Waals energy) were obtained from the work of Aryanpour et al. [49] and Psofogiannakis et al. [63], who developed and used these parameters to model iron-oxyhydroxide systems and hydration of zeolite, respectively. We validated these parameters by comparing ReaxFF-MD simulations of the surface formation energy and water adsorption energy on the Fe(110) surface with DFT calculations [46].

All simulations were performed at room temperature (300 K). Based on the number of atoms used in the simulated electrolyte domain, the density of the simulated electrolyte solution at 300 K was 1.1 g/cm^3 [68]. Nose-Hoover thermostat [69,70] was employed to maintain the prescribed system temperature for the canonical (NVT) ensemble. The variation of pressure during simulations was negligible and remained around 1 atm. The system was relaxed at the beginning of the simulation before applying external electric potential. To reduce the possibility of unintended bond breaking and bond formation during relaxation and after the application of the external electric field, the outermost layer of Fe(110) and the nearest species in the electrolyte were separated initially by 2.5 Å. This distance was intended to be larger than the bond lengths of typical iron oxide/hydroxide species (e.g., FeO, FeOOH, Fe_2O_3, etc.) The Velocity-Verlet time stepping scheme [71] was used with an integration time step of 0.1 fs, and the Maxwell-Boltzmann distribution [72,73] was used to set the initial velocities.

The simulations were run for 500 ps under an external electric field, which was applied following the Stern electrical double layer model [74,75] as shown in Fig. 1. The thickness of the Helmholtz layer was 3 Å, which corresponds to the packed layer of the ions close to the iron surface. The external electric field, which was applied over the solution plus the surface iron atoms, was necessary to overcome the challenges associated with long passivation times of iron in alkaline media under open circuit conditions [11,18,48]. Even with the externally applied electric field, the thickness of the passive film obtained from the simulations was thinner than the films obtained from experiments. If the simulations were continued, we expect that similar passive films, both in thickness and composition, to those obtained from experiments would be achieved. However, the computational time needed to reach comparable states would be too long and impractical. We also studied a range of electric potentials to obtain realistically thick passive films that contain different oxide layers. The results that are presented in this paper were reproducible at applied potentials lower than 30 MeV/cm; however, at a significantly higher computational cost. Simulations

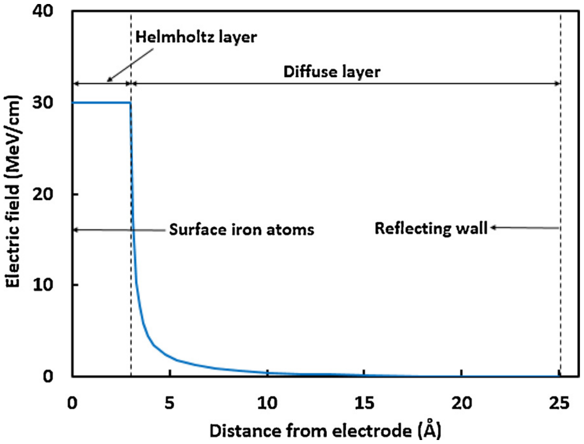

Fig. 1. Applied electric field distribution using the Stern model. Helmholtz and diffuse layers are shown.

under open-circuit conditions (without any applied potential) were not feasible computationally. Larger potentials provided faster film formation; however, we chose to maintain the applied potential as low as practically possible to be close to open-circuit conditions. The application of 30 MeV/cm applied electric field using the Stern model provided a good balance between computational cost and simulation time to study initial stages of passivation. Although increasing the temperature of the system would also accelerate passivation because this increases the diffusion rates of oxygen in iron, the temperature increase would have to be limited in our simulations below the boiling point of the electrolyte, and this level of temperature increase has been shown to have a minor effect on the corrosion process [46]. Therefore, we chose to apply an external electric field to accelerate passivation, which is also a commonly used technique in electrochemical studies [1].

2.2. XPS investigation

XPS scans were performed on circular discs (Ø = 15 mm, thickness = 2 mm) of 99.95% pure iron. Both sides of the discs were polished to 2000 grade silicon carbide paper followed by cloth polishing with 0.3 μm and 0.05 μm alumina suspension in anhydrous isopropyl alcohol (water content: < 0.05% weight). Anhydrous isopropyl alcohol suspension was used in place of a water suspension to minimize surface oxidation during the polishing process. After surface preparation, iron specimens were ultrasonically cleaned, dried and stored in an anaerobic nitrogen chamber to minimize surface oxidation.

A pH 13.5 NaOH (0.316 M) solution was used as the passivating medium. The solution was prepared using analytical grade (99.99%) NaOH and deionized water. Iron specimens were exposed to passivating NaOH solution in a nitrogen chamber to minimize the carbonation of high pH solution in the presence of air. The pH of the solution was continually monitored and was maintained at 13.45 ± 0.05 for the duration of the experiment. Two specimens were taken out of the solution at different passivation times ranging from 10 min to 2 weeks (10 min, 20 min, 30 min, 60 min, 2 days, and 2 weeks.) The long passivation time (2 weeks) was chosen to guarantee full passivation under open circuit conditions [7]. Open circuit potential (OCP) and electrochemical impedance spectroscopy (EIS) measurements confirmed the full passivation of iron specimens after two weeks, as presented in the subsequent sections. Upon removal from the passivating solution, all the specimens were rinsed with anhydrous isopropyl alcohol, dried in a nitrogen chamber, and kept in a nitrogen-filled desiccator. The specimens were prepared and handled with minimum exposure to air and moisture until XPS investigation, when they were only briefly exposed to air during transfer to the nitrogen chamber.

All the specimens were analyzed in angle-resolved XPS, within a few hours of removal from the solution. Specimens were mounted on the specimen holder and subsequently transferred directly to the fore-chamber of the XPS spectrometer and purged with dry nitrogen gas. This chamber was evacuated to $\sim 10^{-6}$Torr before the specimens were transferred to the analytical chamber for examination. The analytical chamber was an ultra-high vacuum (UHV) chamber with a pressure of 10^{-9} Torr. The specimens were analyzed using a Physical Electronics PHI 5600 ESCA system equipped with a monochromatic Al X-ray source (X-ray photon characteristic energy, $h\nu = 1486.6$ eV). The X-ray gun was operated at 300 W (15 kV, 20 mA). The work function of the spectrometer was adjusted using ultra-pure gold metal (Au $4f_{7/2} = 84.0$ eV). The binding scale linearity was set to yield a difference of 848.6 eV between the Cu $2p_{3/2}$ and Au $4f_{7/2}$ photoelectron lines from ultra pure and sputter cleaned Cu, and Au foils. The data were collected using a spherical capacitor analyzer (SCA) equipped with a seven-element "Omni-Focus V" lens. The angle between the analyzer and the X-ray source was 90°. The neutralizing electron gun was not used for analysis since no evidence of surface charging, or charge build-up was observed.

The XPS scans consisted of a survey scan to identify all the species present, followed by high resolutions scans of the species of interest. Survey scans were performed using an energy range of 1440 eV, analyzer pass energy of 187.85 eV, and the step size of 1.6 eV. High-resolution scans were performed using analyzer pass energy of 23.5 eV with a step size of 0.1 eV. High-resolution analyses were calibrated to C 1s (hydrocarbon) signal of 285.0 eV. The high-energy resolution spectra were collected for the elements of interest, which were identified in the survey spectra: oxygen (O 1s), carbon (C 1s), iron (Fe 2p), chlorine (Cl 2p) and sodium (Na 1s). The survey scans and high-resolution scans were performed at an emission angle (θ) of 5°, 25°, 45°, 65° and 85°. The higher the emission angle, the shallower the oxide film depth being analyzed, and hence all the XPS results would be presented in terms of passive oxide film depth.

The XPS data curve fitting and analysis were done using CasaXPS (V 2.3.18PR1.0) data processing software. Shirley background correction procedures and Gaussian (70%)-Lorentzian (30%) function were used for curve fitting procedures of high-resolution spectra. All high-resolution XPS spectra envelopes were smoothed by SG Quadratic method with smoothing width parameter of 21 [76]. The details procedure for the curve fitting process is provided elsewhere [76,77]. Accurate determination of the atomic structure of the oxide film could not be based on the variations of the sodium, carbon and oxygen spectra since these elements are also present in the precipitates from the NaOH solutions on the specimen surface. Despite the best cleaning practices, complete removal of precipitates is not ensured, as the harsh cleaning procedures might damage the oxide film. Since iron is not incorporated into the precipitates, only Fe 2p XPS spectra were used to characterize the oxide films. The film thickness was calculated from the oxide to metal intensity ratios, at an emission angle of 5°, following the procedure described in Ghods et al. [9], assuming a uniform oxide film formation on the iron substrate.

2.3. Electrochemical studies

The same sample polishing procedure described in the XPS study was followed for iron specimens used in the electrochemical tests. All the electrochemical tests were performed in a three-electrode cell with the iron specimen as the working electrode, a graphite rod counter electrode, and a saturated calomel (SCE) reference electrode. The same 0.316 M NaOH aqueous solution (pH = 13.5) used for the XPS investigation was used in the electrochemical testing. Continuous open circuit potential (OCP) measurements were only interrupted by the electrochemical impedance spectroscopy (EIS) scans at regular time intervals (e.g., hourly during the first day and daily during the following days) throughout the test. The frequency scan range for EIS tests was 50,000 Hz to 0.1 Hz, with an AC voltage of 5 mV r.m.s. For the first

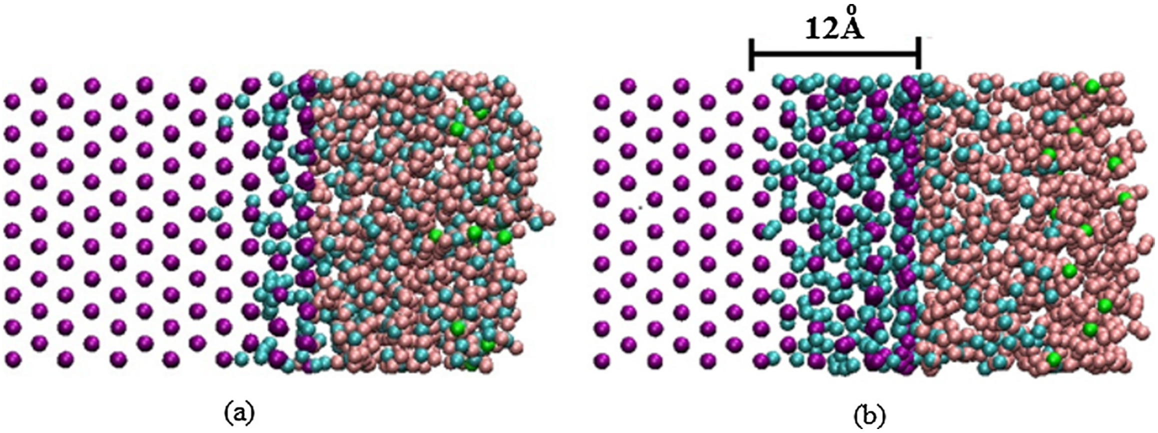

Fig. 2. Snapshots of ReaxFF-MD simulation results of passive film formation at different times: (a) 14 ps and (b) 500 ps. The purple, blue, pink and green spheres represent iron, oxygen, hydrogen and sodium atoms, respectively. (For interpretation of the references to colour in this figure legend, the reader is referred to the web version of this article).

6 h of passivation, the EIS tests were concluded at 0.1 Hz to capture the dynamic changes occurring in a rapidly changing system at early passivation times. For later stages of passivation, the EIS scans continued up to 0.01 Hz. The EIS data were analyzed using equivalent circuit modeling by fitting the data to a Randles circuit that consisted of a resistor representing solution resistance, R_s, in series with a resistor (R_{ct}) and constant phase element (CPE) connected in parallel to represent the electrochemical processes on the iron surface [78]. The simplified Randles circuit has been shown to be a good equivalent circuit model for EIS data for the passive films of iron or carbon steel in high pH electrolytes [11,49,79–83]. We fitted our data to the simplified Randles circuit and other more complex equivalent circuits (e.g. ones with two time constants) and found that the Randles circuit was the most appropriate model for analyzing the EIS data.

3. Results and discussion

3.1. ReaxFF-MD simulations

Fig. 2 presents snapshots of the ReaxFF-MD simulation result of iron in a highly alkaline solution at 14 ps (Fig. 2a), and 500 ps (Fig. 2b). No iron dissolutions into the electrolyte were observed during oxide film formation, indicating iron passivation, unlike earlier simulations on the same iron structure exposed to pure water (pH = 7), which showed iron dissolution and active corrosion [46]. This is expected as iron is known to corrode at neutral pH but passivate in highly alkaline media. The simulations in high pH electrolyte demonstrated that the thickness of the oxide layer and the number of oxygen atoms in the oxide layer increased with time. After 500 ps, the iron oxidation reactions were slow, and the oxygen penetration rate had slowed down to approximately 10% of the initial rate, limiting the growth rate of the passive film.

The initial stages of iron passivation process observed during the simulation are listed below.

Step 1: $OH^-_{(aq)}$ adsorbed on the iron surface, with their oxygen atoms positioned toward iron atoms, forming a FeOH species:

$$Fe_{(s)} + OH^-_{(ads)} \rightarrow FeOH + e^- \quad (1)$$

Step 2: Formation of $Fe(OH)_2$ (Fig. 3a):

$$FeOH + OH^-_{(ads)} \rightarrow Fe(OH)_2 + e^- \quad (2)$$

Step 3: A hydroxide from a $Fe(OH)_2$ reacted with hydrogen from a neighboring $Fe(OH)_2$ species to create a water molecule, which was released into the electrolyte, leaving FeO − OH and FeOH species on the surface. (Fig. 3b):

$$2Fe(OH)_2 \rightarrow FeOOH + Fe(OH) + H_2O_{(l)} \quad (3)$$

Step 4: Oxygen atom, from the FeOOH species, penetrated the iron substrate (Fig. 3c) and oxidized iron in the deeper layers leaving FeOH on the surface.

This oxidation process repeated itself throughout the simulations resulting in a passive film. No iron atom dissolution, into the electrolyte, was observed during the passivation process. The process that led to oxygen diffusion into the iron layers was different from the process that had been observed in simulations in neutral (pH = 7) electrolytes [46]. As shown by Dormohammadi et al. [46], when the electrolyte did not have a reserve alkalinity only the formation of Fe(OH) was observed, but not the $Fe(OH)_2$ layer (as shown in Step 2), which resulted in the dissolution of the iron atoms into the solution while oxygen penetrated into the metal substrate to form mixed oxide. In the high pH electrolyte, as shown in our simulations here, a stable $Fe(OH)_2$ layer was formed creating conditions for oxygen diffusion into the metal without excessive dissolution of iron atoms into the electrolyte. The oxygen penetration, in the absence of iron dissolution or iron vacancy formation, followed by iron oxidation in the metal substrate, is the key step for the formation of the passive film in alkaline environments.

In order to study the composition of the iron passive film that formed during ReaxFF-MD simulations, we compared the Fe-O Pair Distribution Functions (PDF) within the iron oxides with those of Fe-O PDF signature patterns for reference iron oxides identified by Jeon et al. [61], namely, hematite (Fe_2O_3), magnetite (Fe_3O_4) and wustite (FeO). The PDF of Fe_3O_4 has a main peak at 2.0 Å with a slight transition at 1.6 Å, while the main peak of the PDF for Fe_2O_3 occurs at 1.7 Å with a transition at 2.15 Å. The PDF of FeO shows a dominant peak at about 1.65 Å with no transition point. These signatures were used to identify the oxides in the passive film. We tracked the iron oxidation process over time as oxygen atoms penetrated into the iron substrate. We specifically monitored the PDF patterns of the second (Fig. 4a), third (Fig. 4b), and fourth layer (Fig. 4c) by comparing their Fe-O PDF patterns with those of reference oxides.

Fig. 4a shows that the composition of the second iron oxide layer was similar to FeO in the early stages of oxidation (at 14 ps) but changed over time to Fe_3O_4 (at 40 ps), and then to Fe_2O_3 (at 500 ps). These transformations required additional oxygen atoms to penetrate the iron substrate:

$$6\ FeO + 2\ O \rightarrow 2Fe_3O_4 \quad (4)$$

$$4Fe_3O_4 + 2\ O \rightarrow 6Fe_2O_3 \quad (5)$$

For the third and fourth layers, shown in Fig. 4b and c respectively, the composition was transformed from FeO to Fe_3O_4. It is a logical extension of these simulations to assume that in later stages, additional

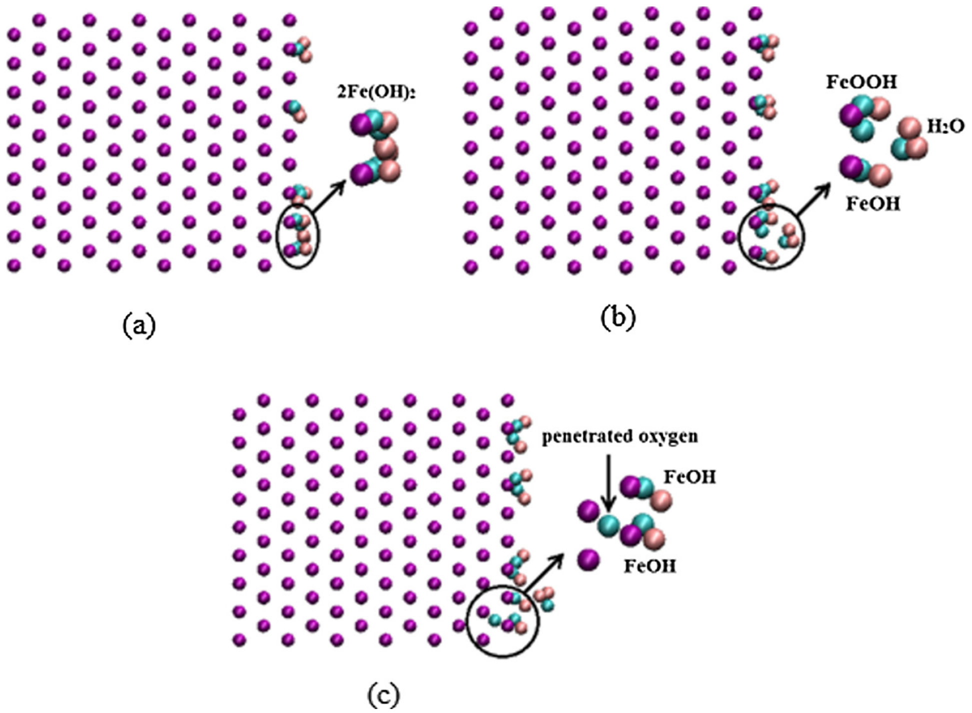

Fig. 3. Key steps of iron passive film formation: (a) the formation of $Fe(OH)_2$; (b) generation of FeO − OH surface species through water formation; (c) oxygen atom penetration into the iron substrate.

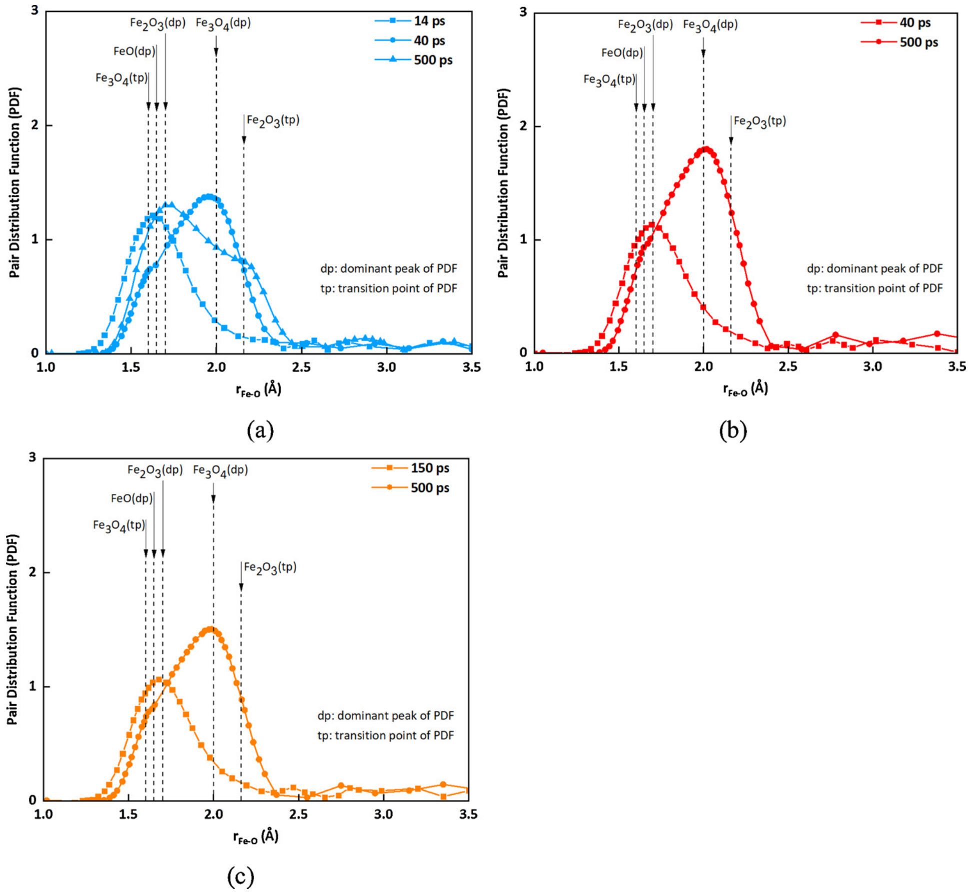

Fig. 4. Pair distribution function of Fe-O at different times for the (a) second iron oxide layer, (b) third iron oxide layer, and (c) fourth iron oxide layer. The dotted lines indicate where one would expect to see the dominant peaks and transition points of the PDF of reference oxides [61].

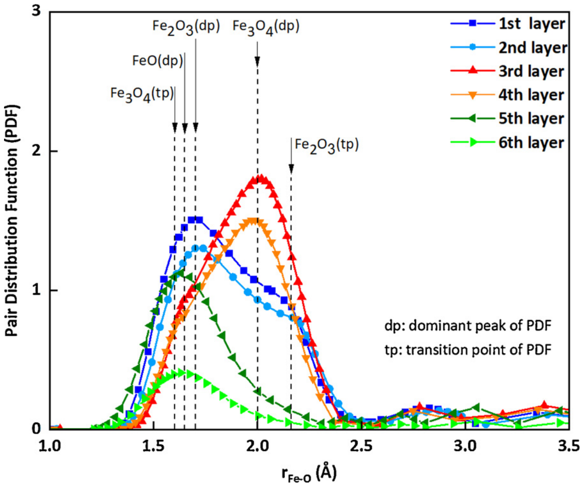

Fig. 5. Pair distribution function of Fe-O for six different iron oxide layers of the passive film at 500 ps. The dotted lines indicate where one would expect to see the dominant peaks and transition points of the PDF of reference oxides [61].

oxygen atoms would penetrate into the passive film, and as a result, the transformation of Fe_3O_4 to Fe_2O_3 would also be observed in these layers.

Fig. 5 shows the Fe-O PDF of the six iron oxide layers at 500 ps, with the “first layer” being the outermost layer on the film/solution interface and the “sixth layer” being the inner layer on the oxide/metal interface. The PDF of the first two outer oxide layers (first and second layers) showed distinct transition points at 2.13 Å and 2.17 Å, while their dominant main peaks were located at 1.71 Å and 1.73 Å, respectively. For the middle two layers (third and fourth layers), the main peaks were at 2.01 Å and 1.98 Å, with slight transitions at 1.67 Å and 1.63 Å. The inner two layers (fifth and sixth layers) showed dominant peaks at 1.66 Å and 1.63 Å, with no transition points. The PDF results of the six oxide layers implied that the compositions of the formed oxide in the two outer oxide layers were similar to Fe_2O_3. While the two middle layers and the two inner layers were similar to Fe_3O_4 and FeO respectively. These results are in agreement with the experimental results of the iron passive film [19,26].

Fig. 6 shows the evolution of oxygen atom density in the iron versus z-distance from the iron/electrolyte interface at 500 ps. The intervals correspond to interlayer spaces of the iron lattice, where oxygen atoms are located. The figure shows how the oxygen atom density decreased progressively with depth, while in an actively corroding system (pH = 7), it peaked in the second layer and decreased in deeper layers [46].

The charge distribution of iron, oxygen, hydrogen, and sodium atoms along the z-direction of the iron in highly alkaline solution at 500 ps are presented in Fig. 7. The six layers of iron atoms in the iron passive film were positively charged with a charge ranging from 0.37e to 0.97e for the first (outermost) sheet, 0.28e to 0.92e for the second sheet, 0.16e to 0.79e for the third sheet, 0.1e to 0.73e for the fourth sheet, 0 to 0.55e for the fifth sheet, and 0 to 0.26e for the sixth sheet. This variability indicates that each depth contained various iron oxide structures. Jeon et al. [61] previously showed that, at 300 K, FeO has the lowest cation and the highest anion charge distribution while Fe_2O_3 has the highest cation and the lowest anion charge distribution. The Fe_3O_4 charge state is an intermediate between FeO and Fe_2O_3. A comparison of charge states of iron atoms in the iron passive film in Fig. 7 with those of reference oxide structures of FeO, Fe_2O_3 and Fe_3O_4 [61] shows that the oxide compositions in the two outermost oxide layers were similar to Fe_2O_3, while the middle and inner layers were similar to Fe_3O_4 and FeO, respectively. The oxide distributions obtained from the charge states matched those predicted by the PDF analysis. These distinct patterns of charge distribution were not observed in the oxide film formed in the simulations of Fe(110) in pure water (pH = 7), rather, a mixed iron oxide formed on the actively corroding surface [46]. The charge of oxygen atoms in the oxidized zone ranged from -0.7e in the outermost layer to -1.0e in the innermost layers, which was not useful in the identification of the oxide structures. Oxygen charge in the electrolyte close to the film surface showed a high degree of variability, which is reflective of the fact that the oxygen atoms within this zone belong to various transitional species that participate in the reactions described in Eqs. 1–3.

3.2. XPS and electrochemical results

The XPS and electrochemical studies were intended to provide support for the ReaxFF-MD simulations. Fig. 8 shows the OCP and EIS measurements for 99.95% pure iron specimens exposed to 13.5 pH NaOH solution as a function of time. Since these experiments were

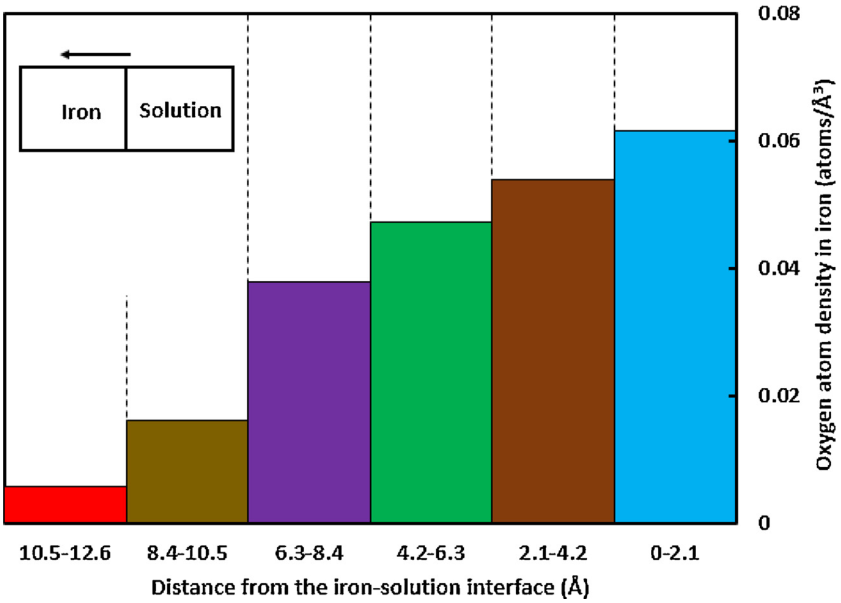

Fig. 6. Oxygen atom density at 500 ps in iron from the iron-solution interface along the z-axis.

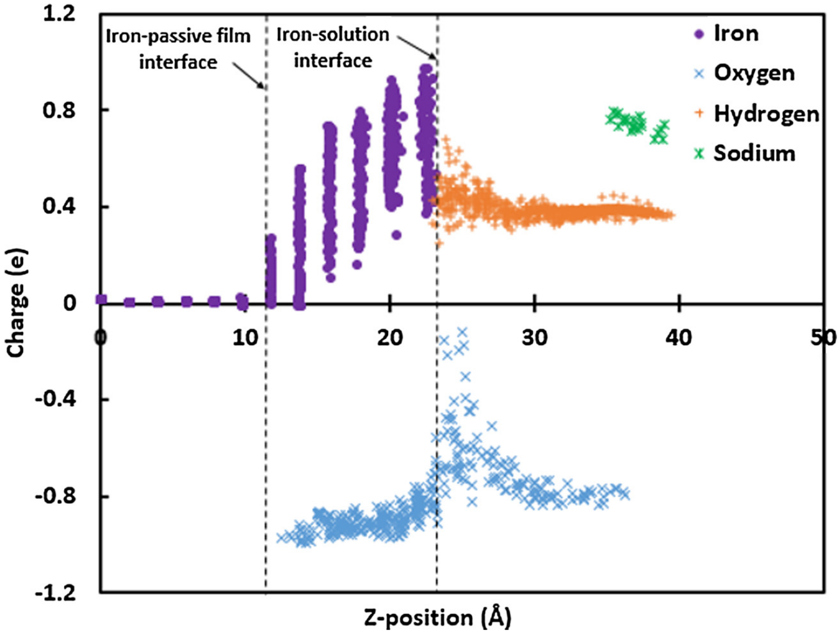

Fig. 7. Charge distributions of the iron, oxygen, hydrogen, and sodium in highly alkaline solution at 500 ps.

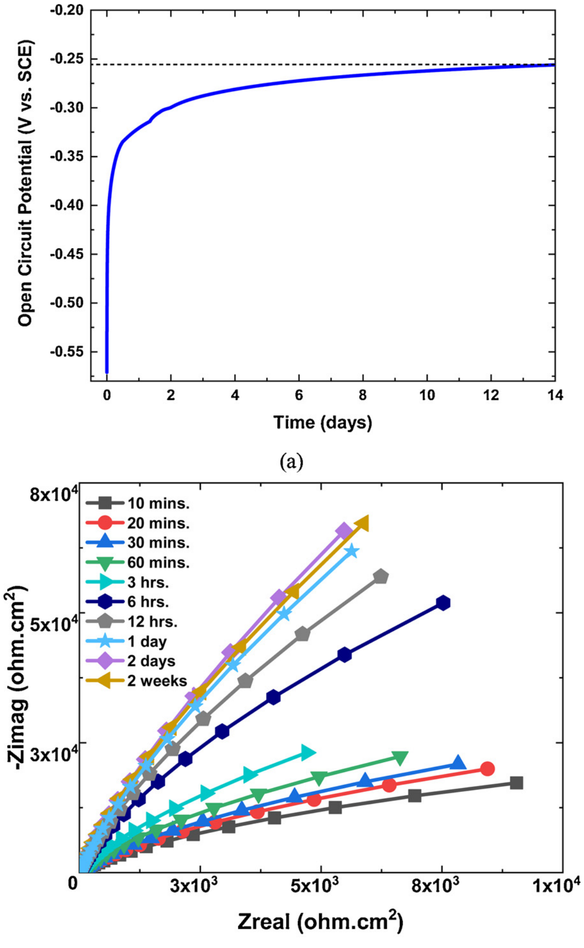

(a)

(b)

Fig. 8. Electrochemical measurements during the 2-week passivation period: (a) open circuit potential; (b) Nyquist plot (For better readability, later stage passivation data (after 6 h) were plotted between 0.1 Hz and 50,000 Hz).

performed without any externally applied potential, the specimens were monitored for two weeks as per the recommendations of prior electrochemical studies of iron and carbon steel in alkaline electrolytes [7]. As shown in Fig. 8, both OCP and EIS measurements indicate that a stable passive film was formed within the first two days of exposure. With increasing passivation time, the OCP increased with time and stabilized around -260 ± 5 mV vs. SCE (shown by the dotted line) after two weeks of exposure (Fig. 8a). The change in OCP was not significant past two days of exposure. Similar conclusions were obtained from the EIS measurements: the impedance data indicate that a stable passive film was obtained after one day of exposure, as shown in Fig. 8b.

We also investigated the build-up of the oxide film with increasing passivation time and oxide film depth using XPS. The composition of the film is presented in terms of the Fe^{III}-to-Fe^{II} oxide concentration ratio. The Fe^{II} oxide state typically covers FeO and Fe_3O_4 oxides, and Fe^{III} oxide state includes α-Fe_2O_3, γ-Fe_2O_3, or FeOOH. Fig. 9a shows the variation of Fe^{III}/Fe^{II} ratio at various film depths at different exposure times. The Fe^{III}/Fe^{II} ratio decreased with increasing oxide film depth for all exposure periods. This change is the result of a decreased amount of Fe^{III} oxides and an increased amount of Fe^{II} oxides from the surface of the passive film to the metal/film interface. These trends indicate that Fe^{III} oxides dominated the outer layers, while Fe^{II} oxides dominated the inner layers of the passive film.

Fig. 9a also shows that both Fe^{II} and Fe^{III} oxide concentrations increased for all layers over time. The increase in Fe^{III} oxide in the outer layers were significantly larger than the increase of Fe^{II} oxide concentration in the inner layers. For the outermost measurement point (0.7 nm from the surface), the Fe^{III}/Fe^{II} ratio increased from 1.7 (at 2 days of exposure) to 3.4 (at 2 weeks of exposure). On the other hand, Fe^{III}/Fe^{II} ratio did not change significantly at the inner measurement points (e.g., at 6 nm or deeper) between two days and two weeks of exposure. The electrochemical data in Fig. 8 shows that passivation was mostly complete after one day of exposure. Therefore, Fe^{III}/Fe^{II} data indicate that Fe^{II} oxides in the inner layers were mainly responsible for the passivation of the iron surface, and the Fe^{III} oxides were not protective [84]. This observation is in line with previous experimental studies [18–20,26] and provides an essential insight into the passivation mechanism of iron in high pH solution.

Fig. 9b illustrates the oxide fraction over the passive film depth after two weeks of exposure to the passivating solution, where the oxide

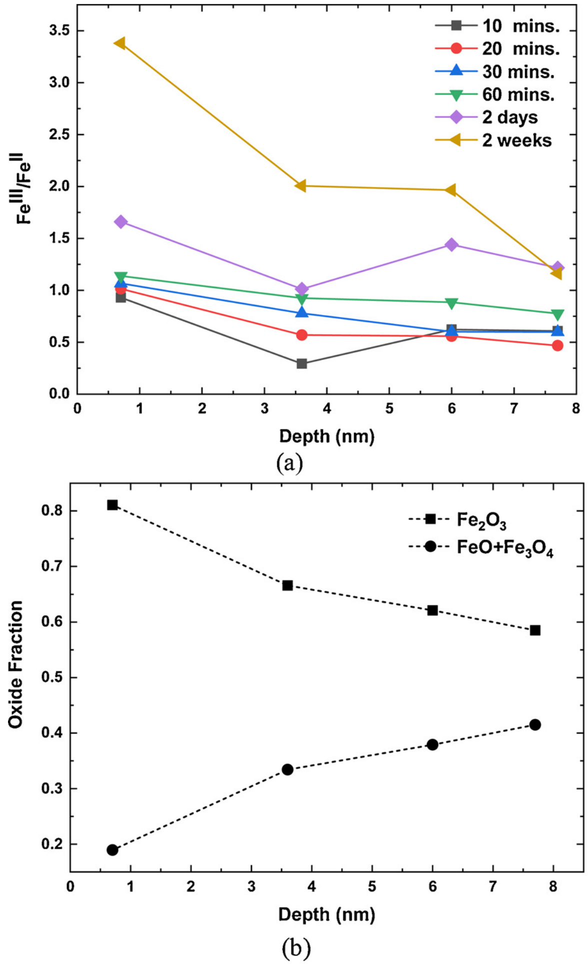

Fig. 9. (a) Fe^{III}/Fe^{II} ratio with increasing passivation time and oxide film depth. (b) Change in oxide phase fractions relative to the total sum of all oxides (i.e., $FeO + Fe_2O_3 + Fe_3O_4$) at full passivation at varying oxide film depth.

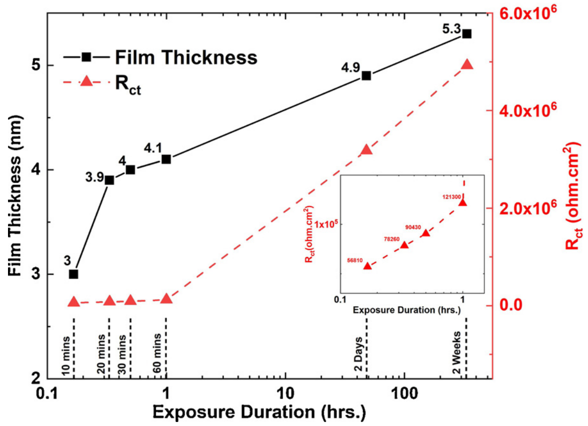

Fig. 10. Variation of oxide film thickness (from the XPS analysis) and charge transfer resistance (from EIS measurements) with increasing exposure duration to the passivating solution. Exposure duration is plotted on a logarithmic scale.

fraction is the ratio of the different oxide phases to the total sum of all oxides (i.e., $FeO + Fe_2O_3 + Fe_3O_4$). The Fe_2O_3 oxide fraction decreased with increasing film depth, whereas, $FeO + Fe_3O_4$ oxide fraction increased with increasing film depth. These two trends reconfirm the abundant presence of Fe^{III} oxides in the outer layers of the passive film and the increasing presence of Fe^{II} oxides closer to the metal/oxide interface. These results confirm the trends obtained from the ReaxFF-MD simulations, which showed that the outer layers of the passive film were similar to Fe_2O_3, and the middle and inner layers were similar to Fe_3O_4 and FeO structures, respectively. It should be noted that the timescales of the ReaxFF-MD and the XPS studies were different. The ReaxFF-MD simulations were performed under an applied electric field for 500 ps to study early stages of passivation, while the XPS study was performed on specimens passivated in open-circuit conditions for two weeks. This resulted in differences in the thickness of the passive films obtained from the two approaches. After two weeks of exposure to the passivating solution, the passive films was about 5.3 nm thick (as shown in Fig. 10), while the passive films created in the ReaxFF–MD simulations under applied potential for 500 ps had a thickness of about 1.2 nm (as shown in Fig. 2b).

The evolution of the thickness and the charge transfer resistance of the passive film is shown in Fig. 10. This figure indicates that an oxide film forms on the iron surface rather rapidly (the thickness was about 3 nm after 10 min exposure to the passivating solution); however, this oxide is not fully passive as indicated by the low charge transfer resistance at 10 min. After two days of exposure to the passivating solution, the thickness of the film has increased slightly to 4.9 nm, while the charge transfer increased by many orders of magnitude to 3.18×10^6 ohm-cm^2. The increase in thickness between 2 days to two weeks was mainly due to the formation Fe^{III} oxides (as indicated by the increase in Fe^{III}/Fe^{II} ratio), which did not change the charge transfer significantly because of their unprotective nature. At full passivation (2 weeks), the average oxide film thickness was 5.3 nm, and the charge transfer resistance was around 4.9×10^6 ohm-cm^2. During the passivation period, the solution resistance, R_s, remained relatively constant between 10–15 ohm.cm^2, which indicates that there was no significant iron dissolution into the electrolyte as expected from a passivating metal.

4. Summary and conclusions

The passivity of Fe(110) in a 0.316 M NaOH solution (pH = 13.5) was investigated using Reactive Force Field Molecular Dynamics (ReaxFF-MD), electrochemical studies, and X-ray photoelectron spectroscopy (XPS). The ReaxFF-MD simulations revealed the initial stages of the iron passivation process, in which passivation was initiated with the formation of $Fe(OH)_2$ species on the metal surface followed by oxygen penetration into the metal substrate. This initiation was different from the process that had been observed in simulations done in neutral (pH = 7) electrolytes [46]. When the electrolyte did not have reserve alkalinity, $Fe(OH)_2$ species did not form, which resulted in the dissolution of the iron atoms into the solution while oxygen penetrated into the metal substrate to form complex oxides. The $Fe(OH)_2$ species that formed and remained on the iron surface created conditions for oxygen diffusion into the metal without excessive dissolution of iron atoms into the electrolyte, hence without iron vacancy formation. The oxygen penetration without iron dissolution or iron vacancy formation, followed by iron oxidation in the metal substrate, was the key step in the formation of the passive film in alkaline environments.

The ReaxFF-MD simulations also showed that the passive film had a layered structure where the outer layers were in the form of Fe_2O_3, middle layers were in the form of Fe_3O_4, and the innermost layers were in the form of FeO.

Parallel XPS and electrochemical investigations confirmed the findings of the ReaxFF-MD simulations. The XPS results showed the dominant presence of Fe^{III} ions (Fe_2O_3 oxide) in the outer regions of the oxide film. However, the Fe^{III} ion concentration decreased with increasing film depth. On the contrary, the Fe^{II} concentration increased with increasing film depth suggesting Fe^{II}-rich inner layers consisting of FeO and Fe_3O_4 oxides closer to the metal/oxide interface. Furthermore, the time-dependent passivation study indicated the transformation of Fe^{II} to Fe^{III} oxides, which was confirmed by increasing Fe^{III} concentration at the top surface of the oxide layer.

Data availability

The raw/processed data required to reproduce these findings cannot be shared at this time as the data also forms part of an ongoing study. Meanwhile raw/processed data will be made available upon request.

Acknowledgments

The study presented in this paper was fully funded by the National Science Foundation, CMMI, Grant No. 1435417. Part of this work used the Extreme Science and Engineering Discovery Environment (XSEDE) Comet at the San Diego Supercomputer Center (SDSC) and Stampede at the Texas Advanced Computing Center (TACC) at the University of Texas at Austin through allocation TG-ENG170002. XSEDE is supported by National Science Foundation grant number ACI-1053575. Part of this research was conducted at the Northwest Nanotechnology Infrastructure, a National Nanotechnology Coordinated Infrastructure site at Oregon State University, which is supported in part by the National Science Foundation (grant NNCI-1542101) and Oregon State University.

References

[1] D.A. Jones, Principles and Prevention of Corrosion, 2nd ed., Prentice Hall, New Jersey, USA, 1996.
[2] R.W. Revie, H.H. Uhlig, Corrosion and Corrosion Control, 4th ed., Wiley-Interscience, New York, 2008.
[3] L. Bertolini, B. Elsener, P. Pedeferri, Rob B. Polder, Corrosion of Steel in Concrete: Prevention, Diagnosis, Repair, Wiley-VCH, Weinheim, 2000.
[4] H. Bohni, Corrosion in Concrete Structures, 1st ed., CRC Press, New York, NY, 2005.
[5] J.P. Broomfield, Corrosion of Steel in Concrete, 2nd ed., (2007).
[6] P.K. Mehta, P.J.M. Monteiro, Concrete: Microstructure, Properties, and Materials, McGraw-Hill Professional., New York, 2005.
[7] P. Ghods, O.B. Isgor, G. Mcrae, T. Miller, The effect of concrete pore solution composition on the quality of passive oxide films on black steel reinforcement, Cement Concrete Comp. 31 (2009) 10.
[8] L. Li, A.A. Sagues, Chloride corrosion threshold of reinforcing steel in alkaline solutions - Cyclic polarization behavior, Corrosion 58 (2002) 12.
[9] C.M. Hansson, A. Poursaee, A. Laurent, Macrocell and microcell corrosion of steel in ordinary Portland cement and high performance concretes, Cement Concrete Res. 36 (2006) 5.
[10] U.M. Angst, B. Elsener, C.K. Larsen, O. Vennesland, Chloride induced reinforcement corrosion: electrochemical monitoring of initiation stage and chloride threshold values, Corros. Sci. 53 (2011) 14.
[11] P. Ghods, O.B. Isgor, G.A. McRae, G.P. Gu, Electrochemical investigation of chloride-induced depassivation of black steel rebar under simulated service conditions, Corros. Sci. 52 (2010) 11.
[12] G.K. Glass, N.R. Buenfeld, The presentation of the chloride threshold level for corrosion of steel in concrete, Corros. Sci. 39 (1997) 13.
[13] L.T. Mammoliti, L.C. Brown, C.M. Hansson, B.B. Hope, The influence of surface finish of reinforcing steel and pH of the test solution on the chloride threshold concentration for corrosion initiation in synthetic pore solutions, Cement Concrete Res. 26 (1996) 6.
[14] L. Li, A.A. Sagues, Chloride corrosion threshold of reinforcing steel in alkaline solutions - Open-circuit immersion tests, Corrosion 57 (2001) 10.
[15] S. Goni, C. Andrade, Synthetic concrete pore solution chemistry and rebar corrosion rate in the presence of chlorides, Cement Concrete Res. 20 (1990) 15.
[16] C. Andrade, C.L. Page, Pore solution chemistry and corrosion in hydrated cement systems containing chloride salts - a study of cation specific effects, Brit. Corros. J. 21 (1986) 5.
[17] U. Angst, B. Elsener, C.K. Larsen, O. Vennesland, Critical chloride content in reinforced concrete - A review, Cement Concrete Res. 39 (2009) 17.
[18] P. Ghods, O.B. Isgor, G.J.C. Carpenter, J. Li, G.A. McRae, G.P. Gu, Nano-scale study of passive films and chloride-induced depassivation of carbon steel rebar in simulated concrete pore solutions using FIB/TEM, Cement Concrete Res. 47 (2013) 14.
[19] P. Ghods, O.B. Isgor, J. Brown, F. Bensebaa, D. Kingston, XPS depth profiling study on the passive oxide film of carbon steel in saturated calcium hydroxide solution and the effect of chloride on the film properties, Appl. Surf. Sci. 257 (2011) 9.
[20] P. Ghods, O. Burkan Isgor, F. Bensebaa, D. Kingston, Angle-resolved XPS study of carbon steel passivity and chloride-induced depassivation in simulated concrete pore solution, Corros. Sci. 58 (2012) 9.
[21] M. Sánchez-Moreno, H. Takenouti, J.J. García-Jareno, F. Vicente, C. Alonso, A theoretical approach of impedance spectroscopy during the passivation ofsteel in alkaline media, Electrochim. Acta 54 (2009) 7222–7226.
[22] M. Sánchez, J. Gregori, C. Alonso, J.J. García-Jareño, H. Takenouti, F. Vicente, Electrochemical impedance spectroscopy for studying passive layers on steel rebars immersed in alkaline solutions simulating concrete pores, Electrochim. Acta 52 (2007) 8.
[23] M. Sánchez, J. Gregori, M.C. Alonso, J.J. García-Jareño, F. Vicente, Anodic growth of passive layers on steel rebars in an alkaline medium simulating the concrete pores, Electrochim. Acta 52 (2006) 7.
[24] D.D. Macdonald, S.R. Biaggio, H.K. Song, Steady-state passive films - interfacial kinetic effects and diagnostic-criteria, J. Electrochem. Soc. 139 (1992) 8.
[25] S. Joiret, M. Keddam, X.R. Novoa, M.C. Perez, C. Rangel, H. Takenouti, Use of EIS, ring-disk electrode, EQCM and Raman spectroscopy to study the film of oxides formed on iron in 1 M NaOH, Cement Concrete Comp. 24 (2002) 9.
[26] H.B. Gunay, P. Ghods, O.B. Isgor, G.J. Carpenter, X. Wu, Characterization of atomic structure of oxide films on carbon steel in simulated concrete pore solutions using EELS, Appl. Surf. Sci. 274 (2013) 8.
[27] C. Colliex, T. Manoubi, C. Ortiz, Electron-energy-Loss-Spectroscopy near-edge fine-structures in the iron-oxygen system, Phys. Rev. B 44 (1991) 10.
[28] A.C.T. van Duin, V.S. Bryantsev, M.S. Diallo, W.A. Goddard, O. Rahaman, D.J. Doren, D. Raymand, K. Hermansson, Development and validation of a ReaxFF Reactive Force Field for Cu cation/water interactions and copper metal/metal oxide/metal hydroxide condensed phases, J. Phys. Chem. A 114 (2010) 9507–9514.
[29] M. Aryanpour, A.C.T. van Duin, J.D. Kubicki, Development of a reactive force field for iron-oxyhydroxide systems, J. Phys. Chem. A 114 (2010) 6298–6308.
[30] D. Raymand, A.C.T. van Duin, D. Spångberg, W.A. Goddard, K. Hermansson, Water adsorption on stepped ZnO surfaces from MD simulation, Surf. Sci. (2010) 741–753.
[31] M.F. Russo, J.R. Li, M. Mench, A.C.T. van Duin, Molecular dynamic simulation of aluminumewater reactions using the ReaxFF reactive force field, Int. J. Hydrogen Energy 36 (2011) 8.
[32] B. Jeon, S.K.R.S. Sankaranarayanan, A.C.T. van Duin, S. Ramanathan, Atomistic insights into aqueous corrosion of copper, J. Chem. Phys. 134 (2011) 234706–234716.
[33] B. Jeon, S.K.R.S. Sankaranarayanan, A.C.Tv. Duin, S. Ramanathan, Reactive molecular dynamics study of chloride ion interaction with copper oxide surfaces in aqueous media, ACS Appl. Mater. Interfaces 4 (2012) 8.
[34] O. Assowe, O. Politano, V. Vignal, P. Arnoux, B. Diawara, V. P, A.C.T. van Duin, Reactive molecular dynamics of the initial oxidation stages of Ni(111) in pure water: effect of an applied electric field, J. Phys. Chem. A 116 (2012) 11796–11805.
[35] O. Verners, A.C.T. van Duin, Comparative molecular dynamics study of fcc-Ni nanoplate stress corrosion in water, Surf. Sci. 633 (2015) 94–102.
[36] C. Zou, Y.K. Shin, A.C.T. van Duin, H. Fangb, Z.K. Liu, Molecular dynamics simulations of the effects of vacancies on nickel self-diffusion, oxygen diffusion and oxidation initiation in nickel, using the ReaxFF reactive force field, Acta. Mater. 83 (2015) 102–113.
[37] T.P. Senftle, S.Y. Hong, M.M. Islam, S.B. Kylasa, Y. Zheng, Y.K. Shin, C. Junkermeier, R. Engel-Herbert, M.J. Janik, H.M. Aktulga, T. Verstraelen, A. Grama, A.C.T. van Duin, The ReaxFF reactive force-field: development, applications and future directions, npj Comput. Mater. 2 (2016) 14.
[38] K. Otte, W.W. Schmahl, R. Pentcheva, Density functional theory study of water adsorption on FeOOH surfaces, Surf. Sci. 606 (2012) 1623–1633.
[39] M.T. Nguyen, N. Seriani, R. Gebauer, Water adsorption and dissociation on alpha-Fe2O3(0001): PBE+U calculations, J. Chem. Phys. 138 (2013) 194709-194701-194708.
[40] Q. Pang, H. DorMohammadi, O.B. Isgor, L. Árnadóttir, Density functional theory study on the effect of OH and Cl adsorption on the surface structure of α-Fe2O3, Comput. Theor. Chem. 1100 (2017) 91–102.
[41] S. Yin, X. Ma, D.E. Ellis, Initial stages of H_2O adsorption and hydroxylation of Fe-terminateda-Fe_2O_3(0 0 0 1) surface, Surf. Sci. 601 (2007) 2426–2438.
[42] A. Soon, M. RTodorova, B. Delley, C. Stampfl, Oxygen adsorption and stability of-surface oxides on Cu(111): a first-principles investigation, Phys. Rev. B - Condensed Matter Mater. Phys. 73 (2006) 1–13.
[43] C.H. Zhang, M. Liu, Y. Jin, D.B. Sun, The corrosive influence of chloride ion-spreference adsorption ona-Al_2O_3(0001) surface, Appl. Surf. Sci. 347 (2015) 386–392.
[44] T. Pan, A.C.T. van Duin, Passivation of steel surface: an atomistic modeling approach aided with X-ray analyses, Mater. Lett. 65 (2011) 4.
[45] T. Pan, Quantum chemistry-based study of iron oxidation at the iron–water interface: an X-ray analysis aided study, Chem. Phys. Lett. 511 (2011) 7.
[46] H. DorMohammadi, Q. Pang, O.B. Isgor, L. Árnadóttir, Atomistic simulation of initial stages of iron corrosion in pure water using reactive molecular dynamics, Comp. Mater. Sci. 145 (2018) 126–132.
[47] M. Balonis, G. Sant, O.B. Isgor, Mitigating steel corrosion in reinforced concrete using functional coatings, corrosion inhibitors, and atomistic simulations, Cem. Concr. Compos. (2018).
[48] A. Poursaee, C.M. Hansson, Reinforcing steel passivation in mortar and ore solution Cem, Concr. Res. 37 (2007) 1127–1134.
[49] H.B. Gunay, O.B. Isgor, P. Ghods, Kinetics of passivation and chloride-induced depassivation of Iron in simulated concrete pore solutions using electrochemical quartz crystal nanobalance, Corrosion 71 (2015) 13.
[50] D.J. Dwyer, S.R. Kelemen, A. Kaldor, The water dissociation reaction on clean and oxidized iron (110), J. Chem. Phys. 76 (1982) 6.
[51] D.J. Dwyer, G.W. Simmons, A study of the initial reaction of water vapor with Fe (001) surface, Surf. Sci. 64 (1977) 16.
[52] S. Hung, W.H. Schwartz, J. Bernasek, Sequential oxidation of Fe (100) by water adsorption: formation of an ordered hydroxylated surface, Surf. Sci. 248 (1991) 11.
[53] M. Eder, K. Terakura, J. Hafner, Initial stages of oxidation of (100) and (110) surfaces of iron caused by water, Phys. Rev. B 64 (2001) 7.
[54] X. Liu, X. Tian, T. Wang, X. Wen, Y. Li, J. Wang, H. Jiao, Coverage dependent water dissociative adsorption on Fe(110) from DFT computation, PCCP 17 (2015) 11.
[55] S. Liu, X. Tian, T. Wang, X. Wen, Y. Li, J. Wang, H. Jiao, Coverage dependent water dissociative adsorption on the clean and O-precovered Fe(111) surfaces, J. Phys. Chem. C 119 (2015) 11.

[56] S. Plimpton, Fast parallel algorithms for short–range molecular dynamics, J. Comput. Phys. 117 (1995) 42.

[57] J. Towns, T. Cockerill, M. Dahan, I. Foster, K. Gaither, A. Grimshaw, V. Hazlewood, S. Lathrop, D. Lifka, G.D. Peterson, R. Roskies, J.R. Scott, N. Wilkins-Diehr, XSEDE: accelerating scientific discovery, Comput. Sci. Eng. 16 (2014) 13.

[58] A.C.T. van Duin, S. Dasgupta, F. Lorant, W.A. Goddard, ReaxFF: a reactive force field for hydrocarbons, J. Phys. Chem. A 105 (2001) 14.

[59] A.C.T. van Duin, A. Strachan, S. Stewman, Q. Zhang, X. Xu, W.A. Goddard, $\text{ReaxFF}_{\text{SiO}}$ reactive force field for silicon and silicon oxide systems, J. Phys. Chem. A 107 (2003) 9.

[60] A.C.T. van Duin, V.S. Bryantsev, M.S. Diallo, W.A. Goddard, O. Rahaman, D.J. Doren, D. Raymand, K. Hermansson, Development and validation of a ReaxFF Reactive Force Field for Cu cation/water interactions and copper metal/metal oxide/metal hydroxide condensed phases, J. Phys. Chem. A 114 (2010) 8.

[61] B. Jeon, Q.V. Overmeere, A.C.Tv. Duin, S. Ramanathan, Nanoscale oxidation and complex oxide growth on single crystal iron surfaces and external electric field effects, J. Chem. Soc. Faraday Trans. 15 (2013) 10.

[62] T.P. Senftle, S. Hong, M.M. Islam, S.B. Kylasa, Y. Zheng, Y.K. Shin, C. Junkermeier, R. Engel-Herbert, M.J. Janik, H.M. Aktulga, T. Verstraelen, A. Grama, A.C.T. van Duin, The ReaxFF reactive force-field: development, applications and future directions, Npj Comput. Mater. 2 (2016) 14.

[63] G.M. Psofogiannakis, J.F. McCleerey, E. Jaramillo, A.C.Tv. Duin, ReaxFF reactive molecular dynamics simulation of the hydration of Cu-SSZ-13 zeolite and the formation of Cu dimers, J. Phys. Chem. C 119 (2015) 9.

[64] O. Verners, A.C.T. van Duin, Comparative molecular dynamics study of fcc-Ni nanoplate stress corrosion in water, Surf. Sci. 633 (2015) 8.

[65] C. Zou, Y.K. Shin, A.C. van Duin, H. Fangb, Z.K. Liu, Molecular dynamics simulations of the effects of vacancies on nickel self-diffusion, oxygen diffusion and oxidation initiation in nickel, using the ReaxFF reactive force field, Acta Mater. 83 (2015) 102–113.

[66] B. Jeon, Q. van Overmeere, A.C.T. van Duin, S. Ramanathan, Nanoscale oxidation and complex oxide growth on single crystal iron surfaces and external electric field effects, PCCP 15 (2013) 10.

[67] M. Aryanpour, A.C.T. van Duin, J.D. Kubicki, Development of a reactive force field for iron-oxyhydroxide systems, J. Phys. Chem. A 114 (2010) 10.

[68] G. Akerlof, G. Kegeles, The density of aqueous solutions of sodium hydroxide, J. Am. Chem. Soc. 61 (1939) 1027–1032.

[69] S. Nose, A molecular dynamics method for simulations in the canonical ensemble, Mol. Phys. 52 (1984) 14.

[70] W.G. Hoover, Canonical dynamics: equilibrium phase-space distributions, Phys. Rev. A 31 (1985) 3.

[71] M.P. Allen, D.J. Tildesley, Computer Simulation of Liquids, 1st ed., Clarendon Press, Oxford, UK, 1987.

[72] R.C. Dunbar, Deriving the maxwell distribution, J. Chem. Educ. 59 (1982) 22–24.

[73] G.D. Peckham, I.J. McNaught, Applications of Maxwell-Boltzmann distribution diagrams, J. Chem. Educ. 69 (1992) 554–559.

[74] O. Stern, The theory of the electrolytic double layer, Zeitschrift für Elektrochemie und Angewandte Physikalische Chemie 30 (1924) 9.

[75] H. DorMohammadi, Investigation of iron passivity and chloride-induced depassivation in alkaline electrolytes using reactive force Field molecular dynamics (ReaxFF-MD), School of Civil and Construction Engineering, Oregon State University, Corvallis, Oregon, 2018, p. 208.

[76] N. Fairely, CasaXPS Manual 2.3.15, ed., C.S. Ltd., 2009, p. 177.

[77] P. van der Heide, X-Ray Photoelectron Spectroscopy: An Introduction to Principles and Practices, (2011).

[78] M.E. Orazem, B. Tribollet, Electrochemical Impedance Spectroscopy, Wiley, 2017.

[79] G. Liu, Y. Zhang, M. Wu, R. Huang, Study of depassivation of carbon steel in simulated concrete pore solution using different equivalent circuits, Constr. Build. Mater. 157 (2017) 357–362.

[80] G. Blanco, A. Bautista, H. Takenouti, EIS study of passivation of austenitic and duplex stainless steels reinforcements in simulated pore solutions, Cem. Concr. Compos. 28 (2006) 212–219.

[81] V. Feliu, J.A. Gonzalez, C. Andrade, S. Feliu, Equivalent circuit for modelling the steel-concrete interface. II. Complications in applying the Stern-Geary equation to corrosion rate determinations, Corros. Sci. 40 (1998) 995–1006.

[82] P. Ghods, O.B. Isgor, G.A. Mcrae, G.P. Cu, Electrochemical investigation of chloride-induced depassivation of black steel rebar under simulated service conditions, Corros. Sci. 52 (2010) 1649–1659.

[83] L. Li, A.A. Sagues, Chloride corrosion threshold of reinforcing steel in alkaline solutions - Open-circuit immersion tests, Corrosion 57 (2001) 19–28.

[84] R.M. Cornell, U. Schwertmann, The Iron Oxides: Structure, Properties, Reactions, Occurrences and Uses, Wiley, 2006.